Determination of Viscous and Thermal Characteristic Lengths in Rigid Porous Materials via Ultrasonic and Brewster Angle Measurements

Christian Meso, Zine El Abiddine Fellah, El Hadji Amadou Diallo, Erick Ogam, Marie Valentin

Determination of Viscous and Thermal Characteristic Lengths in Rigid Porous Materials via Ultrasonic and Brewster Angle Measurements

C. Meso,[a] Z.E.A. Fellah, E.H.A. Diallo, E.Ogam, and M. Valentin

Aix Marseille Univ, CNRS, Centrale Med, LMA, Marseille, France

(Dated: 18 June 2025)

This paper introduces a practical and cost-efficient methodology for independently determining the viscous (Λ) and thermal (Λ') characteristic lengths in rigid-frame porous materials. The proposed approach synergistically combines analytical expressions for transmission and reflection coefficients at high frequencies, derived from the Johnson-Champoux-Allard (JCA) model, with experimental measurements of the magnitudes of transmission coefficients at oblique incidence and Brewster angles. Notably, this method dispenses with a fixed ratio assumption between Λ' and Λ, and does not rely on computationally intensive and noise-sensitive inversion techniques nor on the use of dual-fluid saturation, which may compromise the integrity of the material's microstructure. By incorporating multiple angles of incidence, the method enables the extraction of additional information from the medium, potentially revealing anisotropic or heterogeneous features and thereby improving model accuracy. The experimental setup employs a standard ultrasonic measurement system with a signal generator, two 100 kHz transducers, and a digital oscilloscope. The results obtained for melamine and polyurethane foams, which are widely used in building acoustics and the automotive industry, exhibit overall consistency with values reported in the literature, further supporting the robustness and reliability of the proposed method.

[a] meso@lma.cnrs-mrs.fr

I. INTRODUCTION

The acoustic behavior of porous materials results from complex interactions between the solid skeleton and the saturating fluid, leading to visco-thermal dissipations. These effects are described by the frequency-dependent dynamic tortuosity and dynamic compressibility, which are governed by fluid properties, and characteristic material parameters. In the high-frequency regime, key parameters include porosity ϕ, tortuosity α_∞, viscous characteristic length Λ, and thermal characteristic length Λ'. ϕ quantifies fluid volume, α_∞ captures pore tortuosity (Zwikker and Kosten, 1949), while Λ (Johnson *et al.*, 1987) and Λ' (Champoux and Allard, 1991) respectively characterize viscous dissipation and heat transfer at the fluid-solid interface. Numerous studies have addressed these parameters (Beranek, 1942; Brown, 1980; Carman, 1956; Champoux *et al.*, 1991; Henry, 1997; Johnson, 1986; Johnson *et al.*, 1982; Leonard, 1948; Van Brakel *et al.*, 1981), with this work focusing particularly on the characteristic lengths.

Initially, non-acoustic techniques such as the BET (Brunauer–Emmet–Teller) surface method (Brunauer *et al.*, 1938), based on physico-chemical surface analysis, were used to estimate Λ'. However, this approach was costly and had an uncertainty of around 20%. Image processing techniques also provided only rough estimates for Λ' (Melon, 1996). As a result, researchers turned to acoustic methods, which enable simultaneous measurement of Λ and Λ' with improved accuracy. Notably, Leclaire *et al.* (1996) developed the two-slope method to measure Λ and Λ' under identical conditions, similar to the $Q\delta$ method (Johnson *et al.*, 1987), both relying on different saturating fluids. The two-slope method exploits

differences between air and helium, leveraging high-frequency dispersion curves, while the $Q\delta$ method uses the high-frequency limit of the curves to analyze the product of the quality factor Q and viscous skin depth δ. Although effective, these methods are costly, because of the need for vacuum systems and sensitive experimental conditions, particularly during the air extraction and helium replacement process, which might alter the sample's intrinsic properties.

To address the challenges of using multiple saturating fluids and mitigate the associated risks, several methods have been developed to characterize porous materials saturated with a single fluid (air) in the high-frequency regime, focusing on the reconstruction of transmitted and reflected waves in inverse scattering problems (Bonfiglio and Pompoli, 2013; Fellah *et al.*, 2003a, 2001, 2003b; Fellah, 2000; Fellah *et al.*, 2003c; Fellah and Depollier, 2000, 2001; Fellah *et al.*, 2002, 2003e, 2007b; Ogam *et al.*, 2010; Roncen *et al.*, 2018a,b; Sebaa *et al.*, 2006). It has been shown that using transmitted waves alone can help determine tortuosity and characteristic lengths. In weakly resistive materials, both characteristic lengths can be determined when the reflected wave from the second interface is detectable (Fellah *et al.*, 2003d). However, because of the strong attenuation of reflected waves in many cases, the use of transmitted or reflected modes alone has proven insufficient for full characterization. To overcome this limitation, Fellah *et al.* (2007a) proposed a numerical approach to the inverse problem using a least-squares method that leverages both transmitted and reflected data simultaneously. These approaches, however, relied on the assumption of a fixed ratio Λ'/Λ varies between 1.5 and 3 (Ayrault *et al.*, 1999; Castagnède *et al.*, 2000; Dauchez, 1999; Mareze and Lenzi, 2011; Moussatov *et al.*, 2001), as solving the inverse problem for both

lengths independently was challenging in the case of porous materials saturated by a single fluid, since viscous and thermal effects produce similar influences on the time-domain shape of the transmitted signal (Berger, 2004).

More recently, Groby *et al.* (2010) developed a frequency-domain method that reconstructs the four key parameters without assuming a fixed ratio between Λ and Λ'. This method reconstructs ultrasonic fields reflected and transmitted through a material plate at normal incidence. Equivalent density and bulk modulus are estimated across multiple frequencies from transmission and reflection coefficients, followed by analytical inversion to obtain the final parameters as averages across frequencies. Nevertheless, difficulties are encountered when applying this method to low-resistivity materials, where quasi-null reflected fields complicate reflection coefficient reconstruction, as well as to high-resistivity materials, where transmission coefficient reconstruction becomes challenging.

This study introduces a direct measurement method to determine both characteristic lengths Λ and Λ' without assuming a fixed ratio. The approach leverages analytical formulations of transmission and reflection coefficients at varying incidence angles, using experimental transmission data alongside the Brewster angle. Transmission experiments determine the transmission coefficient magnitude, while reflection experiments estimate the Brewster angle, at which the reflection is minimum. This method offers a cost-effective and practical alternative to inversion techniques, which may sometimes have to overcome challenges such as instability, non-uniqueness of the solution, and high computational costs. By considering the incidence angle corresponding to the Brewster angle in the theoretical reflection coefficient, a linear equation is derived that links Λ and Λ'. Combined with the transmission

coefficient equation, the problem simplifies to solving two equations with two unknowns, removing the need for a fixed ratio between the characteristic lengths, previously essential for analytical solutions. We applied this method to polyurethane and melamine foam samples widely used in the construction and automotive industries. Measurements were primarily made at the central transducer frequency (100 kHz) but are valid across the -12 dB frequency range, spanning 85 to 115 kHz. Presenting the results as a function of the incidence angle could provide deeper insights into material properties, enabling the detection of anisotropy or heterogeneity. This enhances model accuracy, validates material parameters, and ensures practical relevance. The structure of the paper is as follows: Section II presents the wave equation governing wave propagation in homogeneous and isotropic porous materials having rigid frames, incorporating the frequency-dependent dynamic tortuosity and dynamic compressibility. Section III develops the expressions for transmission and reflection coefficients and derives the analytical formulas for determining characteristic lengths. The materials and experimental setup are described in Section IV. Section V provides the results, analysis, and a comprehensive discussion, including perspectives for future research. The main conclusions are summarized in the last section.

II. BACKGROUND ON WAVES IN POROUS MATERIALS WITH A RIGID FRAME

In porous materials, two distinct phases coexist: a solid matrix (frame) and a saturating fluid phase occupying the interconnected pores. The acoustic wave propagation within such media is typically governed by Biot's theory (Biot, 1956a,b, 1962a,b; Biot and Willis, 1957),

which rigorously models the coupled dynamics of both the solid and fluid phases, accounting for their respective deformations. However, when the saturating fluid is of low density—such as air—the acoustic impedance of the solid phase substantially exceeds that of the fluid phase. Consequently, the solid frame exhibits negligible motion under the passage of the acoustic wave, behaving as acoustically rigid. Under these conditions, the equivalent fluid model is appropriate, wherein wave propagation is described by the governing Eqs. 1 and 2 that characterize the effective medium as a homogeneous and compressible fluid. These equations account for both viscous and thermal losses within the porous network, capturing the key mechanisms of wave attenuation and dispersion.

$$\rho_0 \alpha(\omega) \frac{\partial}{\partial t} \langle \vec{v} \rangle = -\vec{\nabla} \langle p \rangle, \tag{1}$$

$$\frac{\beta(\omega)}{K_0} \frac{\partial}{\partial t} \langle p \rangle = -\vec{\nabla} \cdot \langle \vec{v} \rangle, \tag{2}$$

where ω denotes the angular frequency, ρ_0 is the ambient fluid density, and K_0 represents the adiabatic incompressibility modulus of the fluid. The macroscopic averages $\langle \vec{v} \rangle$ and $\langle p \rangle$ integrate local variations in acoustic velocities and pressures, respectively. $\alpha(\omega)$ and $\beta(\omega)$ represent the frequency-dependent dynamic tortuosity and dynamic compressibility, respectively. Specifically, $\alpha(\omega)$ encapsulates the inertial and viscous effects, while $\beta(\omega)$ accounts for the thermal effects associated with acoustic wave propagation. These two functions depend on the intrinsic parameters of the porous material, and numerous theoretical frameworks have been developed to model them, including the Johnson-Champoux-Allard model (Allard and Champoux, 1992; Champoux and Allard, 1991; Johnson *et al.*, 1987), articulated in the following equations:

$$\alpha(\omega) = \alpha_\infty + \frac{2\alpha_\infty}{\Lambda}\left(\frac{\eta}{j\omega\rho_0}\right)^{1/2} + O\left(\frac{1}{\omega}\right) \tag{3}$$

$$\beta(\omega) = 1 + \frac{2\,(\gamma-1)}{\Lambda'}\left(\frac{\eta}{j\omega\rho_0 Pr}\right)^{1/2} + O\left(\frac{1}{\omega}\right) \tag{4}$$

These expressions include the characteristic parameters of the medium: α_∞ (tortuosity), Λ (viscous characteristic length), and Λ' (thermal characteristic length). In this context, η denotes the fluid dynamic viscosity, γ represents the fluid adiabatic index, and Pr indicates the Prandtl number of the fluid. The additional term $O(1/\omega)$ accounts for higher-order corrections at finite frequencies, which become negligible in the high-frequency limit. Eqs. 1 and 2 lead to the spatiotemporal form of the wave equation, governing sound propagation in a rigid-frame porous medium:

$$\Delta p - \frac{\rho_0\alpha(\omega)\beta(\omega)}{K_0}\frac{\partial^2 p}{\partial t^2} = 0 \tag{5}$$

From this equation, the phase velocity c can be expressed as:

$$c = \frac{c_0}{\sqrt{\alpha(\omega)\beta(\omega)}}, \tag{6}$$

where $c_0 = \sqrt{K_0/\rho_0}$ represents the speed of sound in the unbounded fluid.

III. ANALYTICAL DEVELOPMENT OF TRANSMISSION AND REFLECTION COEFFICIENTS AT OBLIQUE INCIDENCE

A. Pressure and velocity fields

Consider an obliquely incident plane wave at an angle θ, as illustrated in Fig. 1, impinging on a rigid-frame porous material sample with a thickness L. The regions are defined as

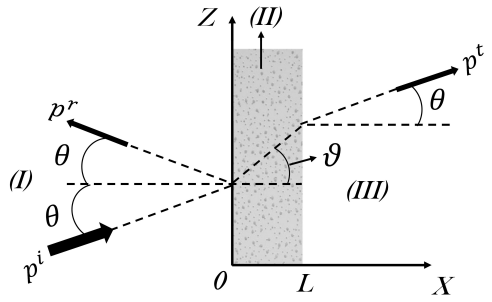

FIG. 1. (Color online) Schematic representation of the geometry involved in the incident wave interaction with the rigid-frame porous material.

follows: Region (I) encompasses the ambient air for $x < 0$; Region (II), for $0 \leq x \leq L$, contains the porous material sample; and Region (III) represents the transmission domain for $x > L$, also filled with air. In Regions (I) and (III), the medium is ambient air, while Region (II) consists of the porous material saturated with air. The pressure field for an incident plane wave with unit amplitude, arriving at an oblique angle to the porous material, is expressed under the $e^{j\omega t}$ time-harmonic convention as:

$$p^i(x,z,t) = e^{-j(k_0 x\cos\theta + k_0 z\sin\theta - \omega t)}. \tag{7}$$

The reflected and transmitted waveforms in regions (I) and (III) are given by:

$$p^r(x,z,t) = Re^{-j(-k_0 x\cos\theta + k_0 z\sin\theta - \omega t)}, \quad p^t(x,z,t) = Te^{-j[k_0(x-L)\cos\theta + k_0 z\sin\theta - \omega t]}, \tag{8}$$

where R and T denote the reflection and transmission coefficients, respectively, and $k_0 = \omega/c_0$ is the wavenumber in free air. For region (II), it has been shown since d'Alembert (1780) that the pressure solution of the wave equation (Eq. 5) can be decomposed into forward- and backward-propagating components:

$$p^{(II)}(x,z,t) = C_1 e^{-j(kx\cos\vartheta + kz\sin\vartheta - \omega t)} + C_2 e^{-j(-kx\cos\vartheta + kz\sin\vartheta - \omega t)}, \tag{9}$$

where ϑ (which should not be confused with the incidence angle θ) is the refraction angle in the porous medium, $k = \omega/c$ is the wavenumber in the porous material, C_1 and C_2 are constants. With the pressure fields known, the corresponding acoustic velocity fields can be readily derived for regions (I), (II), and (III). In region (I), the velocity, as well as the pressure field, results from the superposition of the incident and reflected waves (i.e., $p^{(I)} = p^i + p^r$):

$$v^{(I)}(x,z,t) = \frac{\cos\theta}{Z_0}\left[e^{-j(k_0 x\cos\theta + k_0 z\sin\theta - \omega t)} - Re^{-j(-k_0 x\cos\theta + k_0 z\sin\theta - \omega t)}\right], \tag{10}$$

while in region (II), the velocity field is:

$$v^{(II)}(x,z,t) = \frac{\cos\vartheta}{Z}\left[C_1 e^{-j(kx\cos\vartheta + kz\sin\vartheta - \omega t)} - C_2 e^{-j(-kx\cos\vartheta + kz\sin\vartheta - \omega t)}\right], \tag{11}$$

and in region (III), the transmitted velocity is given by:

$$v^{(III)}(x,z,t) = \frac{\cos\theta}{Z_0} T e^{-j[k_0(x-L)\cos\theta + k_0 z\sin\theta - \omega t]}. \tag{12}$$

In these equations, $Z_0 = \rho_0 c_0$ and $Z = \rho_0\alpha(\omega)c$ represent the characteristic acoustic impedances of the wave in free air and in the porous medium, respectively.

B. Reflection and Transmission Coefficients

To determine the reflection and transmission coefficients, continuity conditions are imposed at the interfaces between the porous medium and regions (I) and (III). At $x = 0$ and $x = L$, the continuity of pressure is given by:

$$p^{(I)}(0^-) = p^{(II)}(0^+), \quad p^{(II)}(L^-) = p^{(III)}(L^+), \tag{13}$$

and the conservation of normal particle velocity by:

$$v_x^{(I)}(0^-) = \phi v_x^{(II)}(0^+), \quad \phi v_x^{(II)}(L^-) = v_x^{(III)}(L^+), \tag{14}$$

where ϕ represents the porosity of the medium. By substituting the velocity and pressure field expressions for each region (Eqs. 7–12) into the continuity equations (Eqs. 13 and 14), we obtain a system of four equations with four unknowns: C_1, C_2, R, and T. These equations can be written in matrix form as:

$$\mathbf{M}.\mathbf{x} = \mathbf{s}, \tag{15}$$

where

$$\mathbf{M} = \begin{pmatrix} e^{-jkz\sin\vartheta} & e^{-jkz\sin\vartheta} & e^{-jk_0z\sin\theta} & 0 \\ e^{-jk(L\cos\vartheta+z\sin\vartheta)} & e^{-jk(-L\cos\vartheta+z\sin\vartheta)} & 0 & e^{-jk_0z\sin\theta} \\ \phi\frac{\cos\vartheta}{Z}e^{-jkz\sin\vartheta} & -\phi\frac{\cos\vartheta}{Z}e^{-jkz\sin\vartheta} & \frac{\cos\theta}{Z_0}e^{-jk_0z\sin\theta} & 0 \\ \phi\frac{\cos\vartheta}{Z}e^{-jk(L\cos\vartheta+z\sin\vartheta)} & -\phi\frac{\cos\vartheta}{Z}e^{-jk(L\cos\vartheta+z\sin\vartheta)} & 0 & \frac{\cos\theta}{Z_0}e^{-jk_0z\sin\theta} \end{pmatrix}, \tag{16}$$

$$\mathbf{x} = (C_1, C_2, R, T)^T, \tag{17}$$

and

$$\mathbf{s} = \left(e^{-jk_0z\sin\theta}, 0, \frac{\cos\theta}{Z_0}e^{-jk_0z\sin\theta}, 0\right)^T. \tag{18}$$

By solving this system in the frequency domain, the results can be developed and expressed in terms of hyperbolic sine and cosine functions as follows:

$$C_1 = \frac{(1+E)\exp(j\omega Lq)}{(1+E^2)\sinh(j\omega Lq) + 2E\cosh(j\omega Lq)}, \tag{19}$$

$$C_2 = -\frac{(1-E)\exp(-j\omega Lq)}{(1+E^2)\sinh(j\omega Lq)+2E\cosh(j\omega Lq)}, \tag{20}$$

$$R = \frac{(1-E^2)\sinh(j\omega Lq)}{(1+E^2)\sinh(j\omega Lq)+2E\cosh(j\omega Lq)}, \tag{21}$$

$$T = \frac{2E}{(1+E^2)\sinh(j\omega Lq)+2E\cosh(j\omega Lq)}, \tag{22}$$

where

$$E = \phi\frac{Z_0\cos\vartheta}{Z\cos\theta}, \quad q = \cos\vartheta\sqrt{\frac{\rho_0\alpha(\omega)\beta(\omega)}{K_0}}, \quad \cos\vartheta = \sqrt{1-\frac{\sin^2\theta}{\alpha(\omega)\beta(\omega)}}. \tag{23}$$

Eqs. 21 and 22 provide the general formulations for the reflection and transmission coefficients, respectively. In Subsection III C, these expressions will be further exploited to derive the analytical formulations required for the determination of the viscous and thermal characteristic lengths.

C. Analytical expressions for characteristic length calculations

By combining the expressions for dynamic susceptibilities (Eqs. 3 and 4) in Eq. 22, and performing a first-order expansion in $1/\sqrt{j\omega}$, the magnitude of the transmission coefficient T can be expressed as:

$$|T| = \left|\frac{4F}{(1+F)^2}\right| \exp\left[-\omega\alpha_\infty\frac{L}{c_0}\frac{\delta}{2}\frac{\left(\frac{1}{\Lambda}+\frac{\gamma-1}{\Lambda'\sqrt{Pr}}\right)}{\sqrt{\alpha_\infty-\sin^2\theta}}\right], \tag{24}$$

where

$$F = \frac{\phi\sqrt{\alpha_\infty-\sin^2\theta}}{\alpha_\infty\cos\theta}, \quad \delta = \sqrt{\frac{2\eta}{\omega\rho_0}}. \tag{25}$$

Here, δ represents the viscous skin depth, a crucial parameter in the acoustics of porous media for distinguishing between high- and low-frequency asymptotic regimes, particularly when compared with the characteristic pore size, "a". If $\delta \ll a$, the system operates in

a high-frequency regime, where viscous effects are confined to a thin fluid layer near the pore walls. Conversely, if δ is comparable to or larger than the pore radius, viscous effects dominate the entire fluid space, which is characteristic of a low-frequency regime.

By further expanding Eq. 24 to isolate terms involving $1/\Lambda$ and $1/\Lambda'$, the equation can be rewritten as:

$$\frac{1}{\Lambda} + \frac{1}{\Lambda'}\frac{\gamma - 1}{\sqrt{Pr}} = \frac{2c_0}{\delta\omega L\alpha_\infty}\sqrt{\alpha_\infty - \sin^2\theta}\ln\left[\frac{4F}{|T|\,(1+F)^2}\right]. \tag{26}$$

The term E^2 in Eq. 21 is of particular interest because, under specific conditions, its value directly influences the reflection coefficient of the medium. In particular, when the incidence angle θ equals the Brewster angle θ_b, the reflection coefficient becomes negligible, which allows the approximation $E^2 \approx 1$. To explore this relationship further, we begin by using the expressions from Eq. 23 in conjunction with those from Eqs. 3 and 4, and perform a first-order expansion in $1/\sqrt{j\omega}$. This leads to an expression for E^2 as the sum of its real and imaginary parts, as shown below:

$$E^2 = \Re\left[E^2\right] + j\Im\left[E^2\right], \tag{27}$$

where:

$$\Re\left[E^2\right] = \frac{\phi^2}{\cos^2\theta}\left\{\left(\frac{1}{\alpha_\infty} - \frac{\sin^2\theta}{\alpha_\infty^2}\right) + \frac{1}{\sqrt{\omega}}\frac{\sqrt{2}}{2}\left[\frac{1}{\Lambda'}\frac{A}{\alpha_\infty} + \frac{B}{\Lambda\alpha_\infty^2}\left(\frac{2\sin^2\theta}{\alpha_\infty} - 1\right)\right]\right\}, \tag{28}$$

$$\Im\left[E^2\right] = -\frac{\phi^2}{\cos^2\theta}\frac{1}{\sqrt{\omega}}\frac{\sqrt{2}}{2}\left[\frac{1}{\Lambda'}\frac{A}{\alpha_\infty} + \frac{B}{\Lambda\alpha_\infty^2}\left(\frac{2\sin^2\theta}{\alpha_\infty} - 1\right)\right]. \tag{29}$$

The constants A and B, introduced to simplify the equations, are given by:

$$A = 2(\gamma - 1)\sqrt{\frac{\eta}{\rho_0 Pr}}, \quad B = 2\alpha_\infty\sqrt{\frac{\eta}{\rho_0}}. \tag{30}$$

Once the relationship for E^2 is derived, we can examine its behavior at the Brewster angle. Substituting the condition $E^2 \approx 1$ in Eq. 27 leads to the following equations (Eqs. 31 and 32), which are essential for further characterizing the material properties:

$$\frac{1}{\Lambda}\frac{\sqrt{2}}{2\sqrt{\omega}}\frac{B}{\alpha_\infty^2}\left(\frac{2\sin^2\theta_b}{\alpha_\infty}-1\right)+\frac{1}{\Lambda'}\frac{\sqrt{2}}{2\sqrt{\omega}}\frac{A}{\alpha_\infty}=\frac{\cos^2\theta_b}{\phi^2}-\left(\frac{1}{\alpha_\infty}-\frac{\sin^2\theta_b}{\alpha_\infty^2}\right), \tag{31}$$

$$\frac{1}{\Lambda}\frac{B}{\alpha_\infty^2}\left(\frac{2\sin^2\theta_b}{\alpha_\infty}-1\right)+\frac{1}{\Lambda'}\frac{A}{\alpha_\infty}=0. \tag{32}$$

In summary, we now have three equations involving two unknowns, Λ and Λ'. The first equation (Eq. 26) is derived from the theoretical expression of the transmission coefficient, while the remaining two (Eqs. 31 and 32) are based on the theoretical expression of the reflection coefficient. However, solving the system comprising Eqs. 31 and 32 alone proves insufficient, as these equations exhibit linear dependence, resulting in an indeterminate system with infinitely many solutions. Thus, the characteristic lengths must be determined by solving either the system formed by Eqs. 26 and 31, or by solving the system of Eqs. 26 and 32.

Solving the system formed by Eqs. 26 and 31 leads to unrealistic results, such as negative characteristic lengths or viscous characteristic lengths greater than thermal characteristic lengths, a situation that contradicts the physical reality of dissipation mechanisms. Indeed, in rigid-frame porous media saturated with fluid, viscous dissipation, which directly depends on friction with the pore walls, occurs on smaller length scales (pore scale) and is therefore more significant than thermal dissipation, which occurs over larger distances.

As will be shown through numerical results in Subsection V B 1, only the system composed of Eqs. 26 and 32 provides realistic and physically meaningful results. Specifically, by solving

Eqs. 26 and 32, we derive the following expressions:

$$\Lambda = \frac{\omega L \delta \left[A\alpha_\infty^5 - B^2 \left(\alpha_\infty - 2\sin^2\theta_b\right)^2 \right]}{2c_0 A \alpha_\infty^2 \sqrt{\alpha_\infty - \sin^2\theta} \ln\left(\frac{|4F|}{|T|(1+F)^2}\right)}, \tag{33}$$

$$\Lambda' = \frac{\omega L \delta \left[A\alpha_\infty^5 - B^2 \left(\alpha_\infty - 2\sin^2\theta_b\right)^2 \right]}{2c_0 B \alpha_\infty^2 \sqrt{\alpha_\infty - \sin^2\theta} \left(\alpha_\infty - 2\sin^2\theta_b\right) \ln\left(\frac{|4F|}{|T|(1+F)^2}\right)}. \tag{34}$$

Eqs. 33 and 34 demonstrate that the viscous and thermal characteristic lengths can be distinctly computed as functions of the other material parameters, the Brewster angle, and the experimentally measured transmission coefficient magnitudes.

IV. MATERIALS AND EXPERIMENTAL SETUP

A. Samples and applications

Four foam samples, as illustrated in Fig. 2 and detailed in Table I, with varying thicknesses, were utilized in this study to collect experimental data. The first sample is a melamine foam, typically employed as a sound absorber in buildings, particularly for thermal insulation and acoustic paneling. Melamine foam is favored in architectural acoustics thanks to its lightweight structure, fire resistance, and high sound absorption coefficients, which makes it well suited for reducing reverberation in large spaces such as auditoriums and concert halls. The remaining three samples consist of polyurethane foams, commonly used as acoustic absorbers in the automotive industry because of their excellent sound attenuation properties across a broad frequency range. These polyurethane foams are particularly effective at reducing noise from engine vibrations and other mechanical sources.

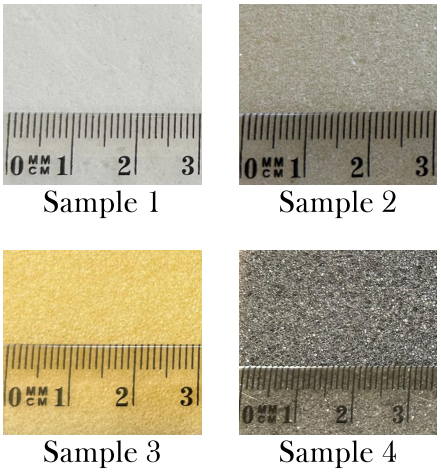

FIG. 2. (Color online) Visualization of samples.

TABLE I. Descriptive information of samples

Sample	Material	Our ref.[a]	Thickness[b] (mm)
Sample 1	Melamine	Mousse ML	30.0
Sample 2	Polyurethane	Mousse F	24.7
Sample 3	Polyurethane	Mousse G	48.7
Sample 4	Polyurethane	Mousse X	30.6

[a] Internal labeling system used by our team for sample identification.

[b] Measured using a caliper with 1/20 vernier scale.

B. Transmission measurement setup

The experimental transmission setup is presented in Figs. 3 and 4. A pulse generator (Sofranel, 5058PR) powers an ultrasonic broadband transducer (Ultran, NCG100-D50) with

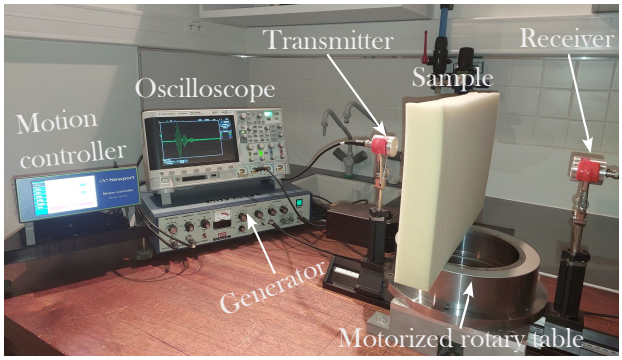

FIG. 3. (Color online) Experimental transmission setup.

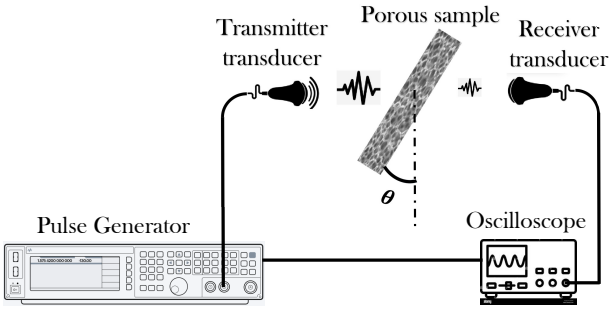

FIG. 4. (Color online) Schematic view of the experimental transmission setup.

a central frequency of 100 kHz. The acoustic wave emitted by the transmitting transducer propagates through the medium and is captured by a second transducer, also operating at 100 kHz and connected to an oscilloscope (Agilent Technologies, DSO-X 3014A) for visualizing and recording the digital signals. To reduce high-frequency noise, the received signals were low-pass filtered at 1 MHz, and electronic interference was minimized by averaging over 6000 acquisitions. Without any sample positioned between the transmitting and receiving transducers, the recorded signal corresponds solely to the incident wave propagating through air. When a sample is introduced between the transducers, the recorded signal is designated as the transmitted signal, representing the acoustic response of the sample.

These responses were measured at various incidence angles θ, ranging from 0 to 60° in 5° increments. For each transmission measurement, the sample was mounted on a motorized rotary table (Newport, RV240CC), controlled by a motion controller (Newport, ESP302). The angle of measurement was limited to 60° to minimize diffraction effects at the sample edges.

C. Reflection measurement setup

Reflection measurements were conducted to determine the Brewster angles for each sample, using the experimental configuration shown in Fig. 5. The results are presented in Section V. The overall setup is similar to the transmission measurement configuration described in Subsection IV B, with the main distinction being that, instead of rotating the sample on a motorized table, the transducers were repositioned to vary the angle of incidence. Another key difference lies in the data acquisition process. To capture the incident signals at different incidence angles θ, a 2.5 cm thick metal plate, assumed to be a perfect reflector, was initially placed to ensure that the receiving transducer detected the maximum reflected signal from the emitting transducer. For the acquisition of the reflected signals from the samples, the metal plate was replaced by the test samples, and measurements were taken at incidence angles ranging from 0° to 60° in 5° increments. These reflected signals represent the acoustic response of the samples during reflection. The transducer positions were adjusted symmetrically with respect to the sample's transverse axis to ensure accurate reflection measurements.

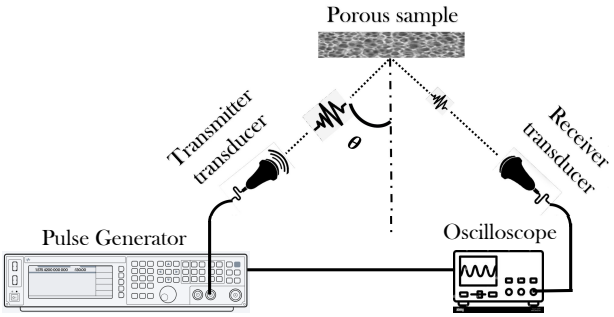

FIG. 5. (Color online) Schematic view of the experimental reflection setup.

V. RESULTS OF ULTRASONIC MEASUREMENTS

A. Analysis of the experimental measurements

1. Representation of signals in the time and frequency domains

Fig. 6 illustrates the incident and transmitted signals at normal incidence for each sample in the time domain. From the sample responses, we first observe amplitude attenuation, indicating their sound absorption capacity and highlighting their practical applications in noise insulation. Additionally, these responses exhibit a time delay, with the red signals consistently arriving later than the blue signals at the receiver. This delay can be physically explained by the acoustic wave encountering a rigid porous material during its propagation. The acoustic motion in the surrounding air is transmitted to the air saturating the material's pores. Because of the rigidity of the solid frame, the motion is confined to the air within the pores. These pores not only possess a tortuous structure but also serve as sites of visco-thermal dissipation, contributing to acoustic energy loss. Consequently, the wave reaches the receiver with a delay after propagating through the porous medium. Tortuosity, an intrinsic

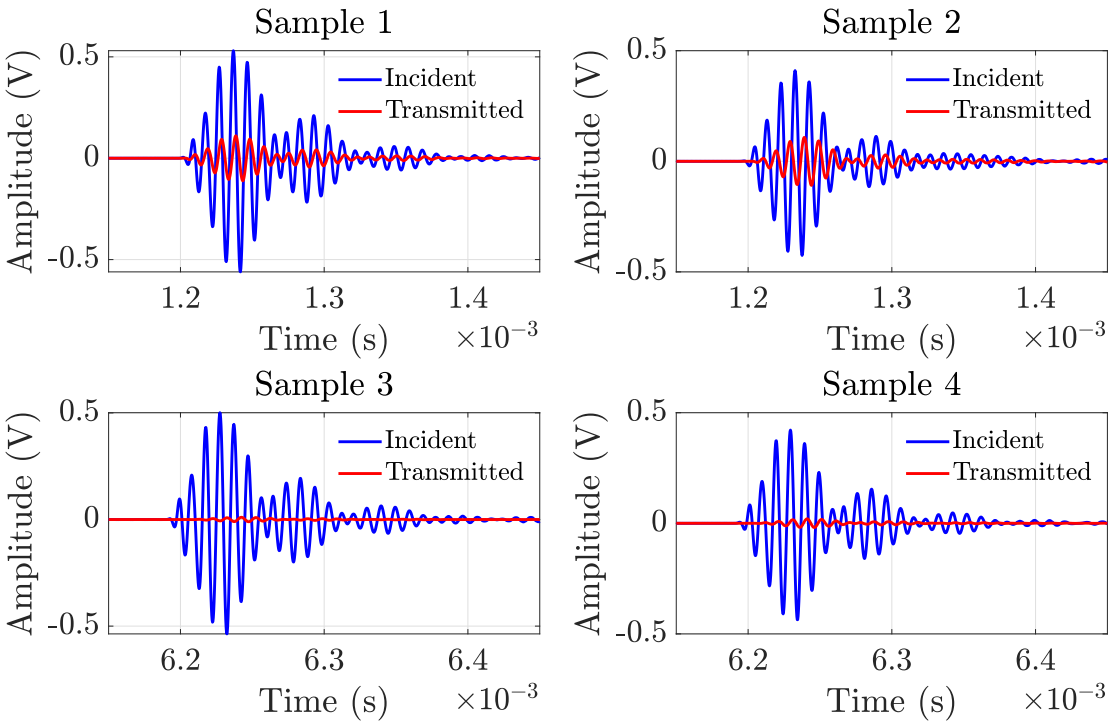

FIG. 6. (Color online) Incident and transmitted signals in the time domain at normal incidence.

property of porous materials, quantifies the complexity of the paths followed by acoustic waves as they propagate through the material. We estimated the tortuosity values for each sample using the method described by Allard *et al.* (1994). The results show that melamine foam (Sample 1) presents the lowest tortuosity $\alpha_\infty \approx 1.03$, implying minimal resistance to acoustic wave propagation. In contrast, Sample 2 exhibits a slightly higher tortuosity ($\alpha_\infty \approx 1.18$), while Samples 3 and 4 reach values of 1.21 and 1.27, respectively. These increased tortuosity values amplify viscous dissipation mechanisms, leading to enhanced acoustic attenuation. Fig. 7 illustrates the amplitude spectrum of the incident signal, during transmission at normal incidence. It is evident that the dominant frequencies cluster around 100 kHz, corresponding to the central frequency of the transducers used in the

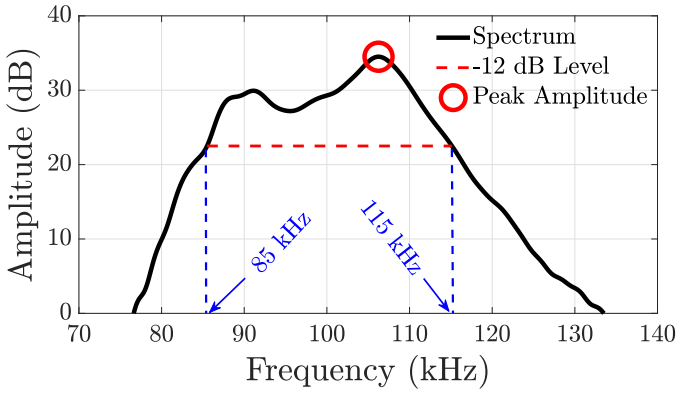

FIG. 7. (Color online) Amplitude spectrum of the incident signal in transmission at normal incidence.

measurements. Based on this observation, we define a relevant frequency band for analyzing the physical phenomena observed in our data. Considering the shape of the amplitude spectrum of the incident signal, we established a frequency range with a lower cutoff at approximately 85 kHz and an upper cutoff at around 115 kHz. These values correspond to the –12 dB level relative to the peak, which encompasses approximately 94% of the total energy. Fig. 8 illustrates the amplitude spectra of the transmitted signals at normal incidence for samples 1, 2, 3, and 4. In addition to the attenuation already observed in their temporal representations, it is noteworthy that the sample responses spectra also exhibit dominant frequencies around 100 kHz. This stability in the central frequency suggests that the materials have not significantly altered the dominant frequency components of the incident wave, indicating minimal frequency dispersion. In other words, while the porous samples have substantially filtered the amplitude of the wave (absorption), they largely preserve the spectral structure of the incident signal. However, this observation holds within the high-frequency (ultrasonic) regime, where viscous and thermal effects are confined to

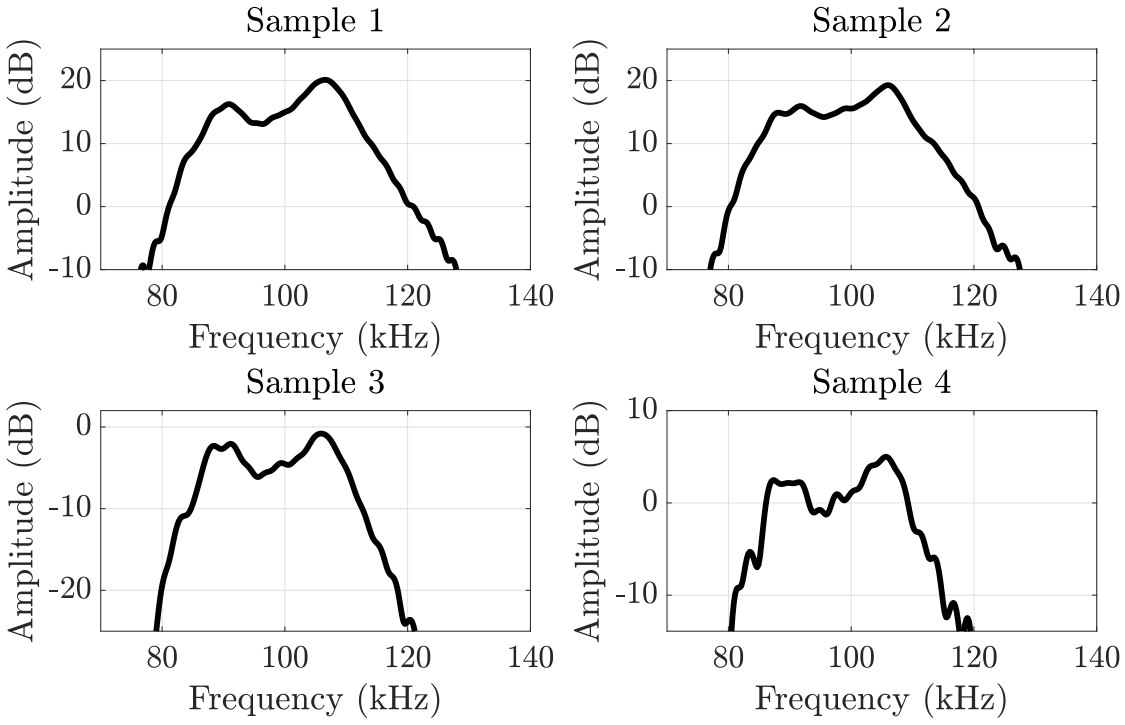

FIG. 8. (Color online) Amplitude spectra of the transmitted signals at normal incidence.

boundary layers near the fluid-solid interfaces, leading to minimal impact on wave dispersion. At lower frequencies (e.g., in the audible range), these effects extend deeper into the fluid domain, enhancing visco-inertial interactions and resulting in more pronounced dispersion.

2. Experimental measurements of the transmission coefficients

The transmission coefficient was assessed through the analysis of the transfer function associated with a linear time-invariant (LTI) system, which quantifies the relationship between incident acoustic pressure and the transmitted acoustic pressure. This coefficient, represented by T, is calculated as the ratio of the cross-spectral power density S_{it} of the incident $p^i(t)$ and transmitted $p^t(t)$ pressures to the auto-spectral power density $S_{ii}(p^i(t))$:

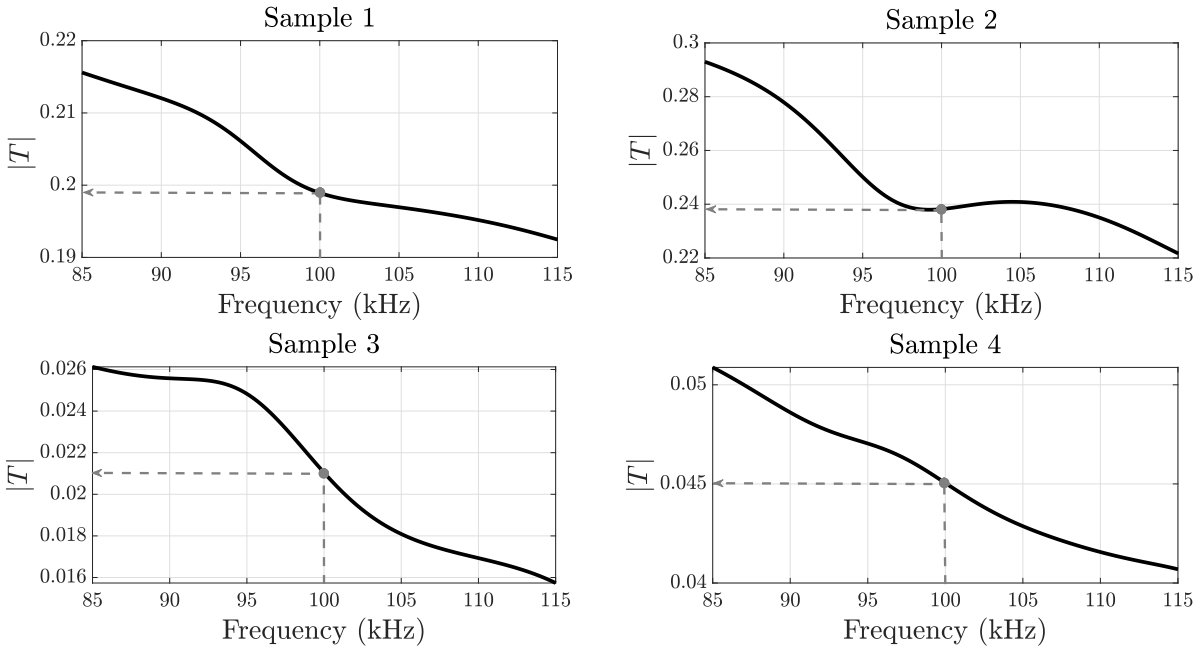

FIG. 9. (Color online) Magnitude of the experimental transmission coefficients at normal incidence.

$$|\widetilde{T}| = \frac{\widetilde{S}_{it}}{\widetilde{S}_{ii}} \tag{35}$$

In this context, the tilde ($\sim$) denotes an estimated function. The magnitude of T was computed utilizing the `tfestimate` function in Matlab®, applied to the acquired signal data. To minimize spectral leakage and enhance the accuracy of spectral measurements, the time-domain signals were pre-processed using windowing techniques, as outlined by MathWorks (2022). For the frequency range between 85 kHz and 115 kHz, Fig. 9 illustrates the magnitude of the experimental transmission coefficients for the different samples at normal incidence. The grey dashed arrows indicate the specific values of $|T|$ selected for subsequent calculations, which correspond to the central frequency of the transducers, namely 100 kHz.

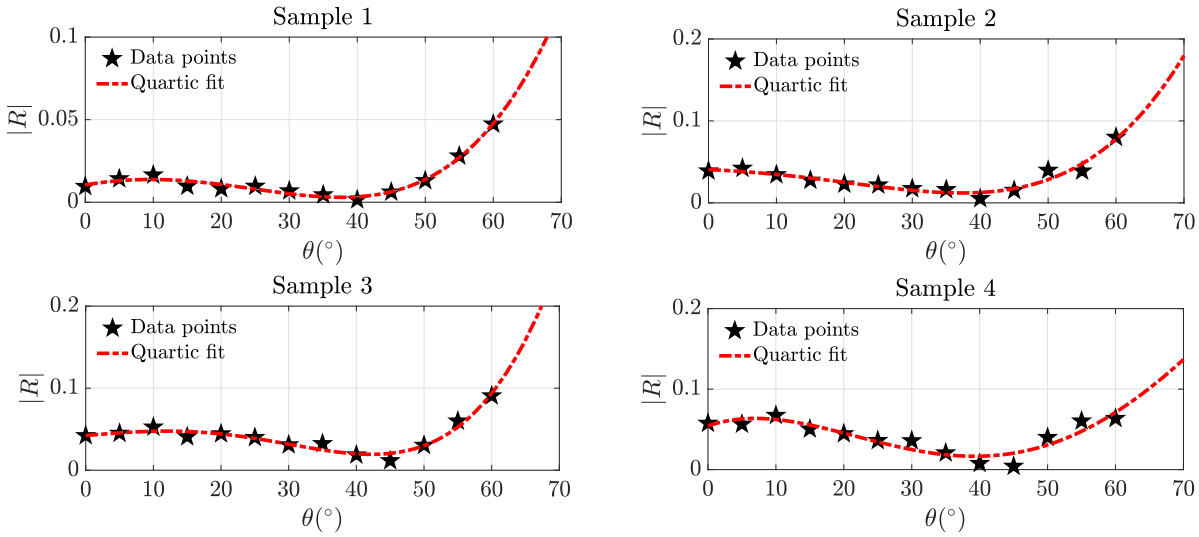

FIG. 10. (Color online) Magnitude of the reflection coefficients.

3. Experimental measurements of the Brewster angles

The experimental work in this paper primarily focuses on transmission measurements. Reflection experiments were conducted exclusively to estimate the Brewster angles, which are essential for deriving the viscous and thermal characteristic lengths in the proposed method. Fig. 10 illustrates the magnitude of the experimental reflection coefficients as a function of the incidence angle θ for each foam sample. The experimental data are represented by black star symbols, while the corresponding fourth-order quadratic regressions, used to capture the global trend, are depicted as red dash-dot lines. The results reveal Brewster angles of approximately 40° for Samples 1 and 2, and about 45° for Samples 3 and 4.

B. Analysis of viscous and thermal characteristic lengths

1. *Determination of the viscous and thermal characteristic lengths*

The results are presented assuming air as the saturating fluid under standard conditions. The following parameter values are used: dynamic viscosity $\eta = 1.839 \times 10^{-5}\,\mathrm{m^2\,s^{-1}}$, fluid density $\rho_0 = 1.213\,\mathrm{kg\,m^{-3}}$, speed of sound $c_0 = 340\,\mathrm{m\,s^{-1}}$, Prandtl number $Pr = 0.71$, and adiabatic index $\gamma = 1.4$. Table II provides a comprehensive summary of the experimental results for each foam sample, as discussed in Subsection V A.

TABLE II: Summary of the experimental measurements.

Sample	Thickness L (mm)	Tortuosity α_∞	$\lvert T\rvert$ (θ=0° at 100 kHz)	Brewster θ_b (°)
Sample 1	30.0	1.03	0.1989	≈ 40
Sample 2	24.7	1.18	0.2381	≈ 40
Sample 3	48.7	1.21	0.0210	≈ 45
Sample 4	30.6	1.27	0.0450	≈ 45

By applying these data to Eqs. 33 and 34, we obtain numerical values for the viscous and thermal characteristic lengths, assuming a porosity of approximately 0.95. It was established (Berger, 2004) that porosity has limited sensitivity in the ultrasonic acoustic wave transmis-

sion. The results for each sample are presented in tables and figures at a frequency of 100 kHz, showing data for various incidence angles θ ranging from 0° to 60° in 5° increments. Additionally, the mean values are also displayed.

a. Results for Sample 1.

TABLE III: Characteristic lengths for Sample 1.

θ	$\|\mathbf{T}\|$ **at 100 kHz**	$\mathbf{\Lambda}$ **(**μ**m)**	$\mathbf{\Lambda'/\Lambda}$
0°	0.19890	145.89 ± 5.69	2.31 ± 0.09
5°	0.19383	144.12 ± 5.62	2.31 ± 0.09
10°	0.19302	145.35 ± 5.67	2.31 ± 0.09
15°	0.18832	145.88 ± 5.69	2.31 ± 0.09
20°	0.18260	147.06 ± 5.74	2.31 ± 0.09
25°	0.16685	144.53 ± 5.64	2.31 ± 0.09
30°	0.15506	145.00 ± 5.66	2.31 ± 0.09
35°	0.14613	148.12 ± 5.79	2.31 ± 0.09
40°	0.12105	143.65 ± 5.63	2.31 ± 0.09
45°	0.10436	144.62 ± 5.67	2.31 ± 0.09

(Continued on next page)

TABLE III – *Continued from previous page*

θ	$\|\mathbf{T}\|$ **at 100 kHz**	$\boldsymbol{\Lambda}$ **(μm)**	$\boldsymbol{\Lambda'/\Lambda}$
50°	0.08598	145.40 ± 5.72	2.31 ± 0.09
55°	0.06552	145.06 ± 5.74	2.31 ± 0.09
60°	0.04320	141.93 ± 5.66	2.31 ± 0.09

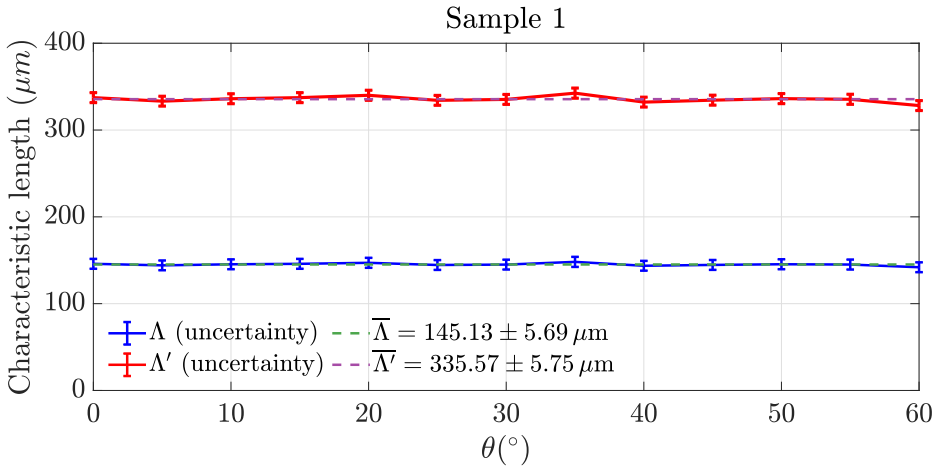

FIG. 11. (Color online) Viscous and thermal characteristic lengths for Sample 1.

b. Results for Sample 2.

TABLE IV: Characteristic lengths for Sample 2.

θ	$\|\mathbf{T}\|$ **at 100 kHz**	$\mathbf{\Lambda}$ **(**μ**m)**	$\mathbf{\Lambda'/\Lambda}$
0°	0.23819	156.15 ± 5.79	1.57 ± 0.06
5°	0.22655	151.35 ± 5.62	1.57 ± 0.06
10°	0.21957	149.64 ± 5.55	1.57 ± 0.06
15°	0.21229	148.76 ± 5.52	1.57 ± 0.06
20°	0.20513	148.87 ± 5.53	1.57 ± 0.06
25°	0.17980	141.53 ± 5.25	1.57 ± 0.06
30°	0.17247	143.35 ± 5.32	1.57 ± 0.06
35°	0.14523	136.36 ± 5.07	1.57 ± 0.06
40°	0.12297	132.18 ± 4.92	1.57 ± 0.06
45°	0.10650	131.27 ± 4.89	1.57 ± 0.06
50°	0.09109	131.29 ± 4.90	1.57 ± 0.06
55°	0.07610	131.76 ± 4.93	1.57 ± 0.06
60°	0.04519	119.19 ± 4.51	1.57 ± 0.06

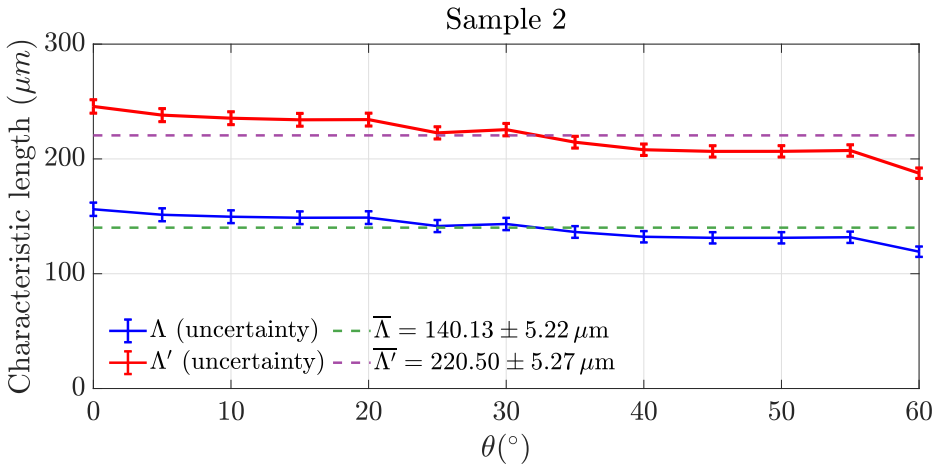

FIG. 12. (Color online) Viscous and thermal characteristic lengths for Sample 2.

366 *c. Results for Sample 3.*

TABLE V: Characteristic lengths for Sample 3.

θ	**|T| at 100 kHz**	**Λ (μm)**	**Λ'/Λ**
0°	0.02101	104.53 ± 4.88	2.69 ± 0.13
5°	0.02209	106.24 ± 4.94	2.69 ± 0.13
10°	0.01757	101.17 ± 4.80	2.69 ± 0.13
15°	0.00632	82.00 ± 4.82	2.69 ± 0.13
20°	0.00757	86.94 ± 4.82	2.69 ± 0.13
25°	0.01587	105.48 ± 5.06	2.69 ± 0.13

(Continued on next page)

TABLE V – *Continued from previous page*

θ	$\|\mathbf{T}\|$ **at 100 kHz**	$\boldsymbol{\Lambda}$ **(μm)**	$\boldsymbol{\Lambda'/\Lambda}$
30°	0.01066	99.72 ± 5.09	2.69 ± 0.13
35°	0.01148	105.80 ± 5.33	2.69 ± 0.13
40°	0.00782	102.39 ± 5.63	2.69 ± 0.13
45°	0.00911	111.93 ± 5.92	2.69 ± 0.13
50°	0.00628	110.65 ± 6.52	2.69 ± 0.13
55°	0.00422	110.31 ± 7.68	2.69 ± 0.13
60°	0.00021	77.18 ± 13.51	2.69 ± 0.13

367

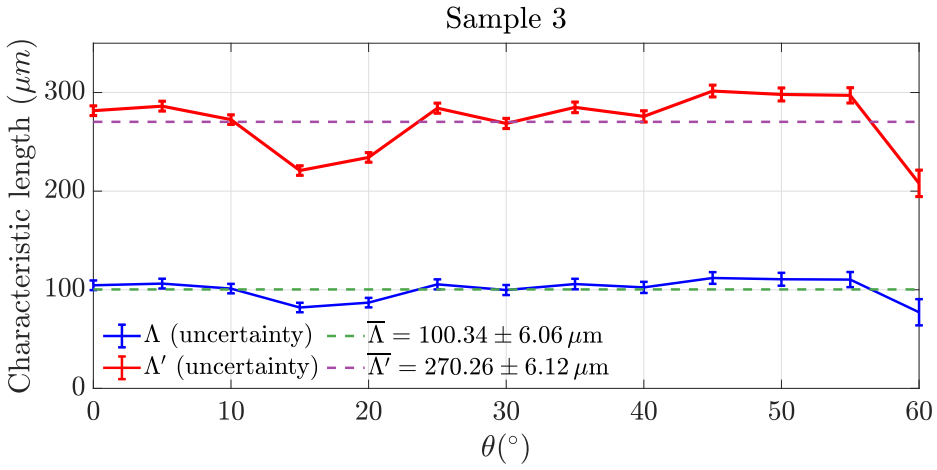

FIG. 13. (Color online) Viscous and thermal characteristic lengths for Sample 3.

368 *d. Results for Sample 4.*

TABLE VI: Characteristic lengths for Sample 4.

θ	$\lvert\mathbf{T}\rvert$ **at 100 kHz**	$\mathbf{\Lambda}$ **(**μ**m)**	$\mathbf{\Lambda'/\Lambda}$
0°	0.04501	86.43 ± 3.82	2.22 ± 0.11
5°	0.04629	87.47 ± 3.86	2.22 ± 0.11
10°	0.04160	85.29 ± 3.78	2.22 ± 0.11
15°	0.03936	85.09 ± 3.78	2.22 ± 0.11
20°	0.03604	84.58 ± 3.77	2.22 ± 0.11
25°	0.02890	81.50 ± 3.67	2.22 ± 0.11
30°	0.02442	80.25 ± 3.66	2.22 ± 0.11
35°	0.01506	74.07 ± 3.55	2.22 ± 0.11
40°	0.00966	70.16 ± 3.67	2.22 ± 0.11
45°	0.01133	76.63 ± 3.86	2.22 ± 0.11
50°	0.00491	68.54 ± 4.57	2.22 ± 0.11
55°	0.00296	66.80 ± 5.90	2.22 ± 0.11
60°	0.00252	69.80 ± 6.84	2.22 ± 0.11

369

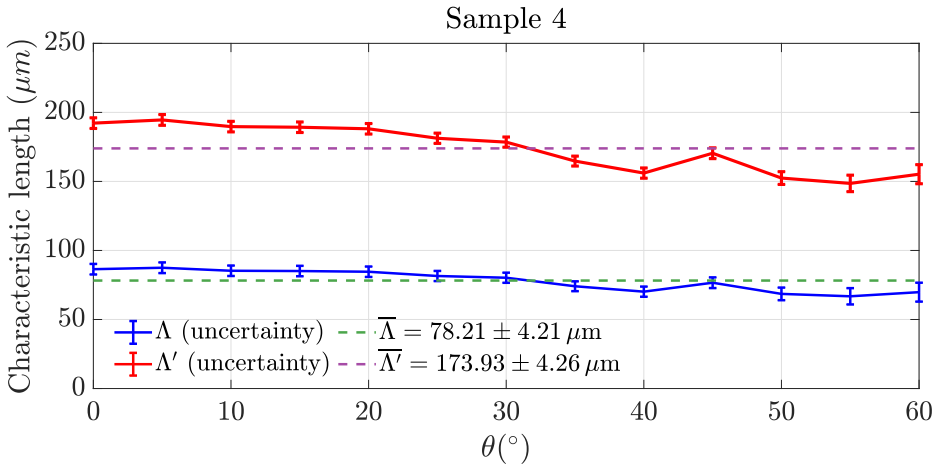

FIG. 14. (Color online) Viscous and thermal characteristic lengths for Sample 4.

Table III and Fig. 11 (along with Table IV and Fig. 12, Table V and Fig. 13, and Table VI and Fig. 14) present the viscous and thermal characteristic lengths at 100 kHz for different incidence angles, derived from the measured transmission coefficients $|T|$ for Samples 1 through 4. Absolute uncertainties in the characteristic lengths were quantified via uncertainty propagation using the differential method applied to Eqs. 33 and 34. Estimated values are ± 0.1, ± 0.01, ± 0.001, $\pm 0.1^\circ$, and $\pm 2^\circ$ for porosity, tortuosity, magnitude of the transmission coefficient, incidence angle, and Brewster angle, respectively. To streamline the derivation, we introduce the notations Z_1, Z_2, and Z_3 to represent respectively the numerator in Eqs. 33 and 34, the denominator of Λ in Eq. 33, and the denominator of Λ' in Eq. 34. The resulting uncertainty expressions, derived via the differential method, are given by:

$$\Delta\Lambda = \left[\frac{1}{Z_1}\sum_{i=1}^{4}|\Delta Z_{1i}| + \sum_{i=1}^{3}\frac{|\Delta Z_{2i}|}{Z_{2i}}\right]\Lambda, \tag{36}$$

$$\Delta\Lambda' = \left[\frac{1}{Z_1}\sum_{i=1}^{4}|\Delta Z_{1i}| + \sum_{i=2}^{3}\frac{|\Delta Z_{2i}|}{Z_{2i}} + \sum_{i=1}^{2}\frac{|\Delta Z_{3i}|}{Z_{3i}}\right]\Lambda, \tag{37}$$

with

$$\Delta Z_{11} = \frac{5|\Delta\alpha_\infty|}{\alpha_\infty} Z_{11}, \quad \Delta Z_{12} = \frac{4|\Delta\alpha_\infty|}{\alpha_\infty} Z_{12}, \quad \Delta Z_{13} = \left(\frac{3|\Delta\alpha_\infty|}{\alpha_\infty} + 2|\Delta\theta_b| \cot\theta_b\right) Z_{13},$$

(38)

$$Z_{14} = \left(\frac{2|\Delta\alpha_\infty|}{\alpha_\infty} + 4|\Delta\theta_b| \cot\theta_b\right) Z_{14}, \quad \frac{\Delta Z_{22}}{Z_{22}} = \frac{1}{\alpha_\infty - \sin^2\theta} \left(|\Delta\alpha_\infty| + |\Delta\theta| \sin 2\theta\right), \quad (39)$$

$$Z_{23} = \ln\left(\frac{4F}{|T|\,(1+F)^2}\right), \frac{\Delta Z_{31}}{Z_{31}} = \frac{3|\Delta\alpha_\infty|}{\alpha_\infty}, \quad \frac{\Delta Z_{32}}{Z_{32}} = \frac{|\Delta\alpha_\infty| + 4|\Delta\theta_b| \cot\theta_b}{\alpha_\infty - 2\sin^2\theta_b} \quad (40)$$

where

$$Z_{11} = \omega L \delta A \alpha_\infty^5, \quad Z_{12} = \omega L \delta B^2 \alpha_\infty^2, \quad Z_{13} = 4\omega L \delta B^2 \alpha_\infty \sin^2\theta_b, \quad Z_{14} = 4\omega L \delta B^2 \sin^4\theta_b,$$

$$\Delta Z_{23} = \frac{|T|\,(1+F)\,|\Delta F| + 2|T|F|\Delta F| + F\,(1+F)\,\Delta|T|}{F|T|\,(1+F)},$$

$$\Delta F = \left[\frac{|\Delta\phi|}{\phi} + \frac{|\Delta\alpha_\infty| + |\Delta\theta| \sin 2\theta}{2\left(\alpha_\infty - \sin^2\theta\right)} + \frac{|\Delta\alpha_\infty|}{\alpha_\infty} + |\Delta\theta| \tan\theta\right] F.$$

It is observed that samples with higher resistance (i.e., those exhibiting greater tortuosity) show lower viscous characteristic lengths. A similar trend is generally noted for the thermal characteristic length. However, this trend exhibits more variability, as the Λ'/Λ ratios derived in this study differ across the materials, suggesting that the expected relationship may not consistently apply to Λ'. For instance, the results indicate that Sample 3 has a higher Λ' than Sample 2, deviating from the anticipated behavior. The larger viscous characteristic lengths in Samples 1 and 2 indicate a dominance of larger pore pathways, resulting in lower viscous dissipation than in Samples 3 and 4, where smaller pores impose stronger viscous constraints. Moreover, the ratio Λ'/Λ remains constant regardless of the incidence angle, even though it varies among the different samples. This constancy can primarily be elucidated by Eq. 32, which shows that this ratio is independent of the angle θ. Instead, it

predominantly depends on the characteristic parameters of the material, the properties of the saturating fluid, and the Brewster angle θ_b.

2. Discussion and perspectives

We identify four observations regarding the viscous and thermal characteristic lengths and their variations as a function of the incidence angle. These insights enhance our understanding of the physical properties of the studied foams and suggest avenues for further research: (i) The results obtained using the method described in this article are presented for a central frequency of 100 kHz, corresponding to the transducers employed in the experiments. However, these results could be extended to reflect frequency-dependent variations. Such analyses would be valuable for characterizing dispersion phenomena in porous media, quantifying the relative contributions of viscous and thermal dissipation across different frequency ranges, and improving the predictive accuracy of acoustic models. (ii) The viscous characteristic lengths obtained are consistent with values typically reported for acoustic foams. The obtained Λ'/Λ ratios align with literature findings for polyurethane foams, which generally range between 2 and 3 (Allard, 1993). However, this range is often cited without explicit physical justification, leaving its underlying mechanisms open to interpretation. Notably, Sample 2 exhibits a lower Λ'/Λ ratio, suggesting a porous structure where viscous and thermal dissipation are more balanced. This warrants further investigation to elucidate the physical basis of such behavior. (iii) The evolution of Λ and Λ' as functions of the incidence angle θ, shown in Figs. 11, 12, 13, and 14, reveals limited variability in the values, supporting the hypothesis of an isotropic and homogeneous medium, as assumed in the

equivalent fluid model used. However, Sample 3, as illustrated in Fig. 12, exhibits greater variation in Λ and Λ' compared with other samples. This variability suggests a higher degree of anisotropy in this foam compared with others, possibly reflecting directional differences in the pore structure that affect visco-thermal dissipation. Additionally, a higher degree of heterogeneity may be present, characterized by irregularities in pore size or shape. Further investigation of this sample could refine the model and enhance the accuracy of predictions. (iv) While the experimental setup used in this study is relatively simple, measurement uncertainties remain inevitable. These uncertainties may arise from various factors, including instrument calibration, geometric deviations such as surface flatness and sample thickness variations, misalignment of sample holders, and numerical data processing. A more detailed uncertainty analysis could be conducted in future studies to further refine the accuracy of the extracted parameters and strengthen the robustness of the conclusions.

VI. CONCLUSION

To circumvent the costly and potentially damaging use of two saturating fluids for determining the viscous (Λ) and thermal (Λ') characteristic lengths, acoustic methods based on solving the inverse scattering problem have been proposed. These methods rely on reconstructing transmitted and/or reflected wave data. However, separating Λ and Λ' remains challenging because of their similar effects on the transmitted signal shape in the time domain. A fixed ratio between the characteristic lengths has been commonly employed to mitigate this sensitivity issue, reducing the number of parameters and the computational burden in the inversion process. In this paper, we introduced a practical and cost-efficient

method to distinctly determine Λ and Λ' without requiring numerical inversion techniques. By leveraging analytical expressions for the transmission and reflection coefficients, along with experimental measurements of the transmission coefficient magnitudes at oblique incidence, we established a solvable system of equations. Specifically, by focusing on the Brewster angle in the theoretical reflection coefficient expression, we derived a linear relation between Λ and Λ', reducing the problem to solving two equations with two unknowns. The method was demonstrated at 100 kHz on melamine and polyurethane foams, which are widely used in building acoustics and the automotive industry. Additionally, presenting results across various incidence angles provided deeper insights into material properties, improving model accuracy, and validating the robustness of material parameters.This approach advances porous material characterization, offering significant improvements in cost, measurement speed, and accuracy, with broad applicability to various industrial sectors.

ACKNOWLEDGMENTS

The first author expresses gratitude to the French Embassy in the Democratic Republic of Congo for their financial support through the "Bourse du Gouvernement Français (BGF)", which made this research possible. Appreciation is also extended to the Polytechnic Faculty of the University of Kinshasa for their valuable assistance during the training.

AUTHOR DECLARATIONS

The authors declare that they have no conflicts of interest to disclose in the context of this research. They also affirm that their work adheres to ethical approval, indicating that their research does not involve experiments on animal subjects and/or human participants.

DATA AVAILABILITY

Data is available upon request from the authors. The information supporting the findings of this study is accessible from the corresponding author upon reasonable request.

Allard, J. F. (**1993**). "Sound propagation in porous materials having a rigid frame," Propagation of Sound in Porous Media: Modelling Sound Absorbing Materials 79–117.

Allard, J. F., Castagnede, B., Henry, M., and Lauriks, W. (**1994**). "Evaluation of tortuosity in acoustic porous materials saturated by air," Review of scientific instruments **65**(3), 754–755.

Allard, J.-F., and Champoux, Y. (**1992**). "New empirical equations for sound propagation in rigid frame fibrous materials," The Journal of the Acoustical Society of America **91**(6), 3346–3353.

Ayrault, C., Moussatov, A., Castagnède, B., and Lafarge, D. (**1999**). "Ultrasonic characterization of plastic foams via measurements with static pressure variations," Ultrasonics **74**, 3224-3226, https://api.semanticscholar.org/CorpusID:121256690.

Beranek, L. L. (**1942**). "Acoustic impedance of porous materials," The Journal of the Acoustical Society of America **13**(3), 248–260.

Berger, S. (**2004**). "Contribution à la caractéristique des milieux poreux par des méthodes acoustiques: estimation des paramètres physiques (Contribution to the Characterization of Porous Media Using Acoustic Methods: Estimation of Physical Parameters)," Ph.D. thesis, Le Mans.

Biot, M. A. (**1956**a). "Theory of elastic waves in a fluid-saturated porous solid. 1. low frequency range," J. Acoust. Soc. Am. **28**, 168–178.

Biot, M. A. (**1956**b). "Theory of propagation of elastic waves in a fluid-saturated porous solid. ii. higher frequency range," The Journal of the acoustical Society of america **28**(2), 179–191.

Biot, M. A. (**1962**a). "Generalized theory of acoustic propagation in porous dissipative media," The Journal of the Acoustical Society of America **34**(9A), 1254–1264.

Biot, M. A. (**1962**b). "Mechanics of deformation and acoustic propagation in porous media," Journal of applied physics **33**(4), 1482–1498.

Biot, M. A., and Willis, D. G. (**1957**). "The elastic coefficients of the theory of consolidation," .

Bonfiglio, P., and Pompoli, F. (**2013**). "Inversion problems for determining physical parameters of porous materials: Overview and comparison between different methods," Acta Acustica united with Acustica **99**(3), 341–351.

Brown, R. J. (**1980**). "Connection between formation factor for electrical resistivity and fluid-solid coupling factor in biot's equations for acoustic waves in fluid-filled porous me-

dia," Geophysics **45**(8), 1269–1275.

Brunauer, S., Emmett, P., and Teller, E. (**1938**). "Absorption of gases in multimolecular layers," J. Am. Chem. Soc. 309–319.

Carman, P. (**1956**). "Flow of gases through porous media" .

Castagnède, B., Aknine, A., Brouard, B., and Tarnow, V. (**2000**). "Effects of compression on the sound absorption of fibrous materials," Applied Acoustics **61**(2), 173-182, https://doi.org/10.1016/S0003-682X(00)00003-7.

Champoux, Y., and Allard, J. F. (**1991**). "Dynamic tortuosity and bulk modulus in air-saturated porous media," Journal of Applied Physics **70**, 1975–1979, https://api.semanticscholar.org/CorpusID:96057102.

Champoux, Y., Stinson, M. R., and Daigle, G. A. (**1991**). "Air-based system for the measurement of porosity," The Journal of the Acoustical Society of America **89**(2), 910–916.

d'Alembert, J. L. R. (**1780**). *Opuscules mathématiques, ou, Mémoires sur différens sujets de geómétrie, de méchanique, d'optique, d'astronomie, &c (Mathematical Opuscules, or, Memoirs on Various Subjects of Geometry, Mechanics, Optics, Astronomy, etc.)*, **8** https://api.semanticscholar.org/CorpusID:117365737.

Dauchez, N. "Étude vibroacoustique des matériaux poreux par éléments finis (Vibroacoustic Study of Porous Materials Using Finite Elements)," Ph.D. thesis, Universite de Sherbrooke, Sherbrooke, Canada, https://api.semanticscholar.org/CorpusID:118261529.

Fellah, Z., Berger, S., Lauriks, W., Depollier, C., and Chapelon, J.-Y. (**2003**a). "Inverse problem in air-saturated porous media via reflected waves," Review of scientific instruments **74**(5), 2871–2879.

Fellah, Z., Depollier, C., and Fellah, M. (**2001**). "Direct and inverse scattering problem in porous material having a rigid frame by fractional calculus based method," J. Sound. Vib **244**(2), 3659.

Fellah, Z., Fellah, M., Lauriks, W., Depollier, C., Chapelon, J.-Y., and Angel, Y. (**2003**b). "Solution in time domain of ultrasonic propagation equation in a porous material," Wave motion **38**(2), 151–163.

Fellah, Z., Mitri, F. G., Fellah, M., Ogam, E., and Depollier, C. (**2007**a). "Ultrasonic characterization of porous absorbing materials: Inverse problem," Journal of Sound and Vibration **302**(4-5), 746–759.

Fellah, Z. E. (**2000**). "Contributiona l'étude de la propagation des onds acoustiques dans les matériaux poreux: approche temporelle," These de doctorat, Université du Maine .

Fellah, Z. E. A., Berger, S., Lauriks, W., Depollier, C., and Fellah, M. (**2003**c). "Measuring the porosity of porous materials having a rigid frame via reflected waves: A time domain analysis with fractional derivatives," Journal of Applied Physics **93**(1), 296–303.

Fellah, Z. E. A., and Depollier, C. (**2000**). "Transient acoustic wave propagation in rigid porous media: A time-domain approach," The Journal of the Acoustical Society of America **107**(2), 683–688.

Fellah, Z. E. A., and Depollier, C. (**2001**). "On the propagation of acoustic pulses in porous rigid media: A time-domain approach," Journal of Computational Acoustics **9**(03), 1163–1173.

Fellah, Z. E. A., Depollier, C., Berger, S., Lauriks, W., Trompette, P., and Chapelon, J.-Y. (**2003**d). "Determination of transport parameters in air-saturated porous materials via

reflected ultrasonic waves," The Journal of the Acoustical Society of America **114**(5), 2561–2569.

Fellah, Z. E. A., Depollier, C., and Fellah, M. (**2002**). "Application of fractional calculus to the sound waves propagation in rigid porous materials: validation via ultrasonic measurements," Acta Acustica united with Acustica **88**(1), 34–39.

Fellah, Z. E. A., Fellah, M., Lauriks, W., and Depollier, C. (**2003**e). "Direct and inverse scattering of transient acoustic waves by a slab of rigid porous material," The Journal of the Acoustical Society of America **113**(1), 61–72.

Fellah, Z. E. A., Fellah, M., Mitri, F., Sebaa, N., Lauriks, W., and Dépollier, C. (**2007**b). "Transient acoustic wave propagation in air-saturated porous media at low frequencies," Journal of Applied physics **102**(8).

Groby, J.-P., Ogam, E., De Ryck, L., Sebaa, N., and Lauriks, W. (**2010**). "Analytical method for the ultrasonic characterization of homogeneous rigid porous materials from transmitted and reflected coefficients," The Journal of the Acoustical Society of America **127**(2), 764–772.

Henry, M. (**1997**). "Mesures des paramètres caractérisant un milieu poreux. etude expérimentale du comportement acoustique des mousses aux basses fréquences (Measurement of Parameters Characterizing a Porous Medium: Experimental Study of the Acoustic Behavior of Foams at Low Frequencies)," Ph.D. thesis, Le Mans.

Johnson, D. L. (**1986**). "Recent developments in the acoustic properties of porous media," Frontiers in Physical Acoustics **93**(1984), 255–290.

Johnson, D. L., Koplik, J., and Dashen, R. F. (**1987**). "Theory of dynamic permeability and tortuosity in fluid-saturated porous media," Journal of Fluid Mechanics **176**, 379 – 402, https://api.semanticscholar.org/CorpusID:123310049.

Johnson, D. L., Plona, T., Scala, C., Pasierb, F., and Kojima, H. (**1982**). "Tortuosity and acoustic slow waves," Physical review letters **49**(25), 1840.

Leclaire, P., Kelders, L., Lauriks, W., Melon, M., Brown, N., and Castagnede, B. (**1996**). "Determination of the viscous and thermal characteristic lengths of plastic foams by ultrasonic measurements in helium and air," Journal of applied physics **80**(4), 2009–2012.

Leonard, R. (**1948**). "Simplified porosity measurements," The Journal of the Acoustical Society of America **20**(1), 39–41.

Mareze, P.H., Lenzi, A.. "Characterization and optimization of rigid-frame porous material," ICSV18, Rio de Janeiro, Brazil, 10–14.

MathWorks, T. (**2022**). *MATLAB version: 9.13.0 (R2022b)* (The MathWorks Inc., Natick, Massachusetts, United States), https://www.mathworks.com.

Melon, M. (**1996**). "Caractérisation de matériaux poreux par ultrasons basse-fréquence (20-500khz) (Characterization of Porous Materials Using Low-Frequency Ultrasound (20-500 kHz))," Ph.D. thesis, Université du Maine.

Moussatov, A., Ayrault, C., and Castagnède, B. (**2001**). "Porous material characterization–ultrasonic method for estimation of tortuosity and characteristic length using a barometric chamber.," Ultrasonics **39**(3), 195–202, https://api.semanticscholar.org/CorpusID:45659775.

Ogam, E., Depollier, C., and Fellah, Z. (**2010**). "The direct and inverse problems of an air-saturated porous cylinder submitted to acoustic radiation," Review of Scientific Instruments **81**(9).

Roncen, R., Fellah, Z., Simon, F., Piot, E., Fellah, M., Ogam, E., and Depollier, C. (**2018**a). "Bayesian inference for the ultrasonic characterization of rigid porous materials using reflected waves by the first interface," The Journal of the Acoustical Society of America **144**(1), 210–221.

Roncen, R., Fellah, Z. E., Lafarge, D., Piot, E., Simon, F., Ogam, E., Fellah, M., and Depollier, C. (**2018**b). "Acoustical modeling and bayesian inference for rigid porous media in the low-mid frequency regime," The Journal of the Acoustical Society of America **144**(6), 3084–3101.

Sebaa, N., Fellah, Z., Fellah, M., Ogam, E., Wirgin, A., Mitri, F., Depollier, C., and Lauriks, W. (**2006**). "Ultrasonic characterization of human cancellous bone using the biot theory: Inverse problem," The Journal of the Acoustical Society of America **120**(4), 1816–1824.

Van Brakel, J., Modrỳ, S., and Svata, M. (**1981**). "Mercury porosimetry: state of the art," Powder technology **29**(1), 1–12.

Zwikker, C., and Kosten, C. (**1949**). *Sound absorbing materials* (Elsevier Amsterdam).